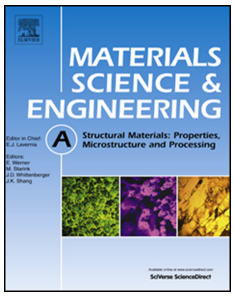

Effects of process parameters, debinding and sintering on the microstructure of 316L stainless steel produced by binder jetting

Nora Lecis, Marco Mariani, Ruben Beltrami, Lorena Emanuelli, Riccardo Casati, Maurizio Vedani, Alberto Molinari

PII: S0921-5093(21)01372-1

DOI: https://doi.org/10.1016/j.msea.2021.142108

Reference: MSA 142108

To appear in: *Materials Science & Engineering A*

Received Date: 1 July 2021

Revised Date: 21 September 2021

Accepted Date: 23 September 2021

Please cite this article as: N. Lecis, M. Mariani, R. Beltrami, L. Emanuelli, R. Casati, M. Vedani, A. Molinari, Effects of process parameters, debinding and sintering on the microstructure of 316L stainless steel produced by binder jetting, *Materials Science & Engineering A* (2021), doi: https://doi.org/10.1016/j.msea.2021.142108.

CRediT authorship contribution statement

Nora Lecis: Conceptualization, Investigation, Supervision, Writing – review and editing.

Marco Mariani: Conceptualization, Investigation, Formal analysis, Writing – original draft.

Ruben Beltrami: Investigation.

Lorena Emanuelli: Investigation, Data curation.

Riccardo Casati: Investigation, Writing – review & editing.

Maurizio Vedani: Supervision, Formal analysis, Writing – review & editing.

Alberto Molinari: Supervision.

Effects of process parameters, debinding and sintering on the microstructure of 316L stainless steel produced by Binder Jetting

Nora Lecis[a], Marco Mariani[a]*, Ruben Beltrami[a], Lorena Emanuelli[b], Riccardo Casati[a], Maurizio Vedani[a], Alberto Molinari[b]

[a] Department of Mechanical Engineering, Politecnico di Milano, Via Privata Giuseppe La Masa 1, 20156 Milano – Italy

[b] Department of Industrial Engineering, University of Trento, Via Sommarive 9, 38123 Trento - Italy

* Corresponding author: marco.mariani@polimi.it

Abstract

Binder Jetting is becoming increasingly important in the scenario of metal Additive Manufacturing processes due to the absence of rapid melting and solidification steps that can induce defects in most sensitive alloys and lead to unwanted reactions. However, this technology requires to consider the effects of different factors such as powder packing, wettability with the binder and sinterability to define suitable process parameters and to achieve desirable material properties. Although several research works focus on individual aspects of Binder Jetting and sintering of parts, a comprehensive understanding of material evolution under different processing conditions has not been achieved yet.

The present research explores the effects of different process and thermal parameters on the porosity and mechanical properties of binder jetted 316L samples. The effect of layer thickness and binder saturation, considering the powder bed features, and debinding and sintering atmospheres, referring to the post-processing stages, were investigated at the green and sintered stages via microstructural and compositional analysis and mechanical characterization. Thermal treatments simulations were employed to determine the microstructural evolution during sintering. The 316L steel produced in this work by Binder Jetting exhibited a fine equiaxed microstructure, tensile strength values comparable to those of cast products and superior ductility compared to other additive techniques.

Keywords: Binder Jetting; Additive Manufacturing; 316L Stainless Steel; Mechanical Properties; Simulation; Phase Transformation.

1 Introduction

Binder Jetting (BJ) is an Additive Manufacturing powder bed process developed at MIT in the early 1990s. It is receiving particular interest from the scientific and industrial communities since it allows extending the advantages of the complex-shape design offered by Additive Manufacturing to a wider class of materials, because it does not involve melting and rapid solidification steps, that can induce defects in the most sensitive alloys and lead to unwanted reactions [1,2].

BJ consists of the deposition of liquid binder micro-droplets to selectively join powder particles of a powder bed, and to enable the creation layer by layer of near-net shaped parts [3]. After printing, the next steps involve curing of the binder, de-powdering of green bodies and sintering of components. In contrast to other powder bed processes that apply laser or electron beam to melt the materials, no heating to the melting stage is involved in BJ process.

Due to this feature, BJ presents remarkable advantages in comparison with other Additive Manufacturing processes and an increasing interest for this technique is growing for industrial applications [4–7]. It allows, in principle, to produce parts from almost any powdered feedstock material, from metals to ceramics, since there are no restrictions regarding high melting points, reflectivity, etc. [8–14]. Considering that the printing process is performed at room temperature, no effect about thermal conductivity needs to be considered and concerns like presence of residual stresses, part distortions or crack formation are significantly reduced. No building support structures are required since there is no need to bear solidification strains, nor to dissipate heat [15,16], density can be flexibly controlled by tuning the post-processing parameters [4], and higher amount of powder can be reused compared to L-PBF or EBM [17,18].

On the other hand, some downsides need to be mentioned. Among them, the additional steps of the post-processing must be considered, which include de-binding and sintering, that are necessary to obtain final objects with suitable strength. Thermo-chemical treatments can generate shrinkage and distortion of the parts, which are still difficult to predict with high accuracy. Moreover, the post-processing treatment parameters must be optimized according to the different combinations of powder and binder and a deeper knowledge on their effects is required to improve product quality and reliability.

Several researchers investigated the effects of different processing parameters on various properties of the final parts. Even if the field of printing parameters is very wide, including layer thickness, binder deposition speed, binder saturation, roll speed, drying time, and others, layer thickness and binder saturation are often considered as the main parameters [19–21].

During printing, the binder is dropped according to the binder saturation (or printing saturation), defined as the ratio between the deposited binder volume and the powder bed voids volume, which usually has a beneficial effect on the green part strength and its safe handling [22]. Some authors suggested that an increase of layer thicknesses and binder saturation leads to a reduction of mechanical properties and geometrical resolution. This is due to two competitive mechanisms: binder spreading and binder infiltration [23,24]. The first consists of the diffusion of the liquid on the layer surface due to capillary pressure; the latter regards the vertical penetration promoted by capillarity and gravity. Good geometrical accuracy and sufficient inter-layer adherence of the green parts can be assured only if binder motion sideward is not excessive, and the powders show suitable wettability. This is strictly dependent on the printing bed packing, which is affected by a series of factors related both to powder properties and printing parameters [25–27].

With the aim of presenting an effective overview, the materials used and the processing parameters reported in relevant studies are summarized in Table 1.

Table 1 Schematic representation of literature contents for different materials and most considered BJ parameters

Material group	Alloy	Avg. Particle Size	Binder Saturation	Layer Thickness	Curing	Debinding	Sintering	Additives	Final Density	Ref.
		μm	%	μm					%	
Stainless Steel	316L	-	-	-	-	-	2h, 1380°C, H_2	-	95-96	[28]
	316L	-	-	50	-	-	-	-	97	[6,29]
	316L	14-31-78	100	150	2h, 200°C	1h, 500°C	1.5h, 1300°C, Ar	-	80	[30]
	316L	4-14-30-82	60	100	2h, 195°C	2h, 460°C	6h, 1350°C, vacuum	BN, B, BC	99	[31,32]
	316L	22	60	50-100	4h, 185°C	1h, 800°C	1h, 1360°C, 95%Ar+5% H_2	nylon	94	[33]
	316	multiple	60	75-100	2h, 180°C	0.5h, 900°C	1.5h, 1435°C, H_2	-	99	[34]
Inconel	625	11	-	-	-	-	2h, 1310°C, vacuum	-	-	[35]
	625	33	-	-	175°C, vacuum	-	4h, 1280°C, vacuum	-	99	[36]
	625	34.5	-	100	175°C	-	4h, 1300°C, vacuum	-	99	[37]
	718	70-7	70-80	-	-	0.5h, 700°C	5h, 1300°C	-	-	[38]
Titanium	Ti	75	-	100	1h, 70°C	-	2h, 1350°C, Ar	-	porous	[39]
	Ti CP	75-90	-	80-150	-	3h, 295°C	1400°C, Ar	-	porous	[40]
Copper	Cu CP	5	-	50		1h, 450°C	3h, 900°C, H_2	-	91	[12]
	Cu CP	multiple	100	80-150	185°C	0.5h, 450°C	2h, 1060°C	-	60-80	[41]
	Cu CP	multiple	100	70	-	0.5h, 450°C	3h, 1075°C, Ar + HIP	-	99	[42]
Composite	SS420 + bronze	10	-	100	2h, 200°C	-	96%Ar+4%H_2	11% bronze	98	[43]

Looking at the density achieved in the finished parts, it seems that currently titanium and copper alloys do not easily reach near full density values as opposed to nickel and iron alloys. Sometimes density values for the same alloy might differ significantly because the samples are produced with different printing parameters and sintering cycles. In this regard, the improvements in sintered

density are often achieved owing to the presence of additives, boron-based or silicon nitride, in particular when it comes to iron-based alloys [44].

The measured shrinkage after debinding and sintering usually ranges from 5 to 20% depending on the material and the process parameters. Titanium presents the lower values, around 5%, nickel and copper-based alloys have a similar shrinkage behavior, that varies between 15 and 20%. Iron-based alloys are peculiar since their volume reduction can vary within a wide range, from 5 to 17%, meaning that these alloys are deeply affected by process parameters, probably more than others [45].

Among all the materials, the most extensively investigated alloy in literature is the AISI 316L stainless steel. To the authors' knowledge, the research works of Do et al. [31,32], Ziaee et al [33] and Verlee et al [34] provide extensive information related to process parameter and resulting properties. In Table 1, the major studies dealing with BJ manufacturing of 316L stainless steel were presented, summarizing the selected printing parameters and thermal treatments. Table 2 further shows the influence of these parameters on the specific properties measured in each paper.

Table 2 Summary of the articles studying the effect of material, and process parameters on the mechanical properties of 316L stainless steel by BJ

	Final density	**Shrinkage**	**Mechanical properties**	**Microstructure**
Powder size and shape	[30–34,46]	[31,33]	[34]	[30]
Sintering cycle	[31,32,34,46]	[45]	[6,31,34]	[6,31,32,46,47]
Additives	[31–33]	[31,33]	[31,32]	[31]
Binder saturation	-	-	[48]	-
Orientation, layer thickness	[28,29]	-	[28,29,48]	[28,29]

From Table 2 it appears that in the literature, the influence of particle size distribution (PSD) and powder morphology on part density is one of the most studied aspects for BJ of 316L stainless steel. To investigate the effect of powder on the final density, batches with different PSD are considered and subjected to the same processes, from printing to sintering. Do et al. [31,32] concluded in their papers that the mixture of two batches with different powder size resulted in an improvement of the packing density up to 70%. Besides, the effect of the particle shape must be taken into account because the sintered part porosity increases by decreasing the sphericity of the feedstock [34].

Limited reports are, however, available on the effect of the microstructure evolution on the mechanical properties of sintered parts. Shrestha et al. [48] considered the influence of binder saturation and printing parameters on the transverse rupture strength (TRS) of 316L binder jetted samples. Do et al. [31] focused on the effect of additives and sintering cycle on material hardness and

tensile strength. Verlee et al. [34] evaluated the ultimate tensile strength (UTS) and fracture elongation in order to investigate the influence of different particle powder sizes. The fatigue behavior of BJ 316L has been reported in a very recent paper by Kumar et al. [28]. From the survey of the open literature, it appears that an exhaustive understanding of the main powder features and processing parameters on the achieved microstructure and properties of BJ 316L steels is still lacking.

In the present research we describe the effects of printing parameters and thermal treatments on the sintering mechanisms, thus on the microstructure, of a 316L stainless steel and we report the possible consequences of the microstructural changes on mechanical properties, as bending strength, tensile properties, and micro-hardness. The focus is placed on layer thickness and binder saturation, which are present on any BJ machine regardless of the manufacturer and size, and they are pivotal to the organic binder distribution homogeneity within the powder bed, therefore in the green and sintered components. In addition, we demonstrate the feasibility of achieving almost full density and excellent mechanical properties, on par with literature results, without the need of sintering aids and reducing atmosphere.

2 Materials and Methods

2.1 Powder material

The feedstock powder used in this experimental work was a gas atomized 316L stainless steel supplied by Sandvik AB with spherical shape (circularity$_{10}$ = 89%) and a unimodal particles size distribution (d_{10} = 2.1 μm, d_{50} = 3.8 μm, d_{90} = 7.8 μm). The chemical composition is reported in Table 3.

Table 3 Chemical composition (wt.%) of the investigated stainless steel AISI 316L powder

	C	O	Si	Cr	Mn	Fe	Ni	Mo
316L	0.03	0.21	0.58	18.28	2.19	65.73	10.90	2.12

2.2 Printing process

Samples were produced with an Innovent+ 3D BJ system manufactured by ExOne (Huntington, PA, US). The binder was a standard aqueous-based type BA-005 solution provided by ExOne containing ethylene glycol monobutylether (EGBE), isopropanol (IPA), and ethylene glycol (EG). The first two constituents evaporate during the curing while the ethylene glycol cross-links producing PEG [32].

The adopted printing parameters are reported in Table 4. They have been selected based on previous experience [49] and were kept constant for all the samples here presented. Instead, the effect of different layer thickness (LT) and binder saturation (BS) values were investigated. LT was considered at two levels, 50 μm and 100 μm, whereas BS was set at 55% or 70%.

Table 4 Constant printing process parameters

Drying time	Bed temperature	Recoat speed	Roller rotation speed	Roller transverse speed
s	°C	mm s^{-1}	rpm	mm s^{-1}
12	55	100.0	600	5.0

The curing process was carried out at 180 °C for 6 hours in air in a YAMATO DX 412 furnace and it was followed by de-powdering via manual brushing and vacuum cleaning, whereas the debinding step was performed in Ar atmosphere in a CARBOLITE 12/75/700 tube furnace at a temperature of 470 °C for 4 hours. The temperatures for the sintering cycle were based on suggested cycles provided by the BJ system manufacturer. Sintering was therefore performed in vacuum by using a HTS HT-S1 LPC vacuum furnace (10^{-1} mbar) at 1360 °C for 3 hours, with a heating rate of 5 °C min^{-1}, followed by a cooling stage with a N_2 pressure of 1.5 bar and an initial cooling rate of -500 °C min^{-1}. During sintering, samples were placed on alumina holders to avoid contamination from the support plate of the furnace.

Samples with different geometries were produced for 3-point bending tests and tensile tests in accordance with the ASTM standards B312-20 and E8/E8M, respectively. For tensile tests, three standard flat unmachined specimens for powder metallurgy were produced for each condition (central width = 5.7 mm), printed with the flat surface parallel to the powder layer.

2.3 Phase formation simulation

To better understand the phase transformations during sintering, CALPHAD-based simulation by ThermoCalc AB Software (Version 2020b, Stockholm, Sweden) were performed under equilibrium hypothesis [50]. The thermodynamic equilibrium and phase stability predictions were evaluated by using the TCFE9 Steel/Fe-alloy database. To improve the accuracy of the results obtained, the specific carbon content of the debinded samples was measured through LECO analyzer according to the ASTM E1019.

Information on post-printing treatments were obtained by thermogravimetric analysis (TGA) performed on pure binder samples using temperature scans from 0 °C to 1000 °C with a 5 °C min^{-1} heating rate, and on green samples from 0 °C to 500 °C with a 5 °C min^{-1} heating rate, both in air and in slightly reducing (95%Ar/5%H_2) atmospheres. The measurements were performed on pre-solidified binder by curing at 190 °C for 2 hours. In these analyses, a slightly reducing atmosphere was adopted to safely eliminate any risk of oxidation processes, while argon atmosphere was employed during debinding to study an easily reproducible treatment at the industrial level.

Additional differential scanning calorimetry (DSC) was performed by a Setaram Labsys 1600 (Lyon, France) on debinded specimens from the four printing combinations, with a heating rate of 5 °C min^{-1} from 20 to 1360 °C, a holding time of 3 hours and a cooling rate of -30 °C min^{-1}.

2.4 Microstructural and mechanical characterization

Microstructural observations were conducted by a field-emission scanning electron microscope (FE-SEM) ZEISS SIGMA 500 equipped by energy dispersive X-ray (EDX) detector by Oxford Inc. SEM investigations were performed on specimens after mirror polishing and chemical etching (H_2O:HCl:HNO_3 1:1:1, according to ASTM E407-07 standard) to study their microstructural properties and on the fracture surfaces of tensile specimens to determine the failure mechanisms. EDX analyses were conducted on mirror polished and chemically etched samples sections to determine the distribution of chromium, nickel and molybdenum. The average grain size was determined by line-intercept method, according to the ASTM E112-13. EDX analyses were conducted on polished surfaces to determine the elemental composition of the phases and inclusions identified in the samples.

XRD analyses for phase identification were performed by SmartLab II Rigaku diffractometer on the polished surface of all samples within a range of 30 – 100°, at a scanning rate of 1° min^{-1}, a step size of 0.01° and a Cu-Kα radiation source (λ = 1.5406 Å).

Samples density was derived by area fraction measurement acquired by image analyses on samples collected both at the green and sintered stages and by the Archimedes' principle (ASTM B962-17) on sintered samples only, since the open porosity of the green samples was excessively large to produce accurate estimates.

Linear shrinkage was evaluated in the three different directions (X = Powder spreader axis, Y = Printhead movement axis, Z = Building direction axis) by measuring three bending test specimens size with a digital caliper after sintering.

Vickers hardness (HV) was measured by microhardness indentation (ASTM B933-20) on polished sectioned samples, close to their surface and in their central regions. The applied load was 100 g_f for a duration of 15 s. Data are obtained by averaging 10 measurements in different areas of the sintered samples. Transverse rupture strength was measured by three-point bending tests on both green (ASTM B312-20, thin configuration) and sintered (ASTM B528-16, thin configuration described in ASTM B925-15) specimens performed by an MTS SYNERGIE 200 testing frame at a loading rate of 90 N min^{-1}. In both cases, the load was applied in the transverse direction with respect to the layer orientation.

Finally, tensile tests were performed on standard flat unmachined test specimens for powder metallurgy products (ASTM E8/E8M, "dogbone" configuration described in ASTM B925-15) by an MTS ALLIANCE RT 100 testing frame, at a strain rate of 1.3 mm min^{-1}. The tensile stress was applied in the parallel direction with respect to the layer orientation to allow a comparison with the best performing specimens produced by other techniques.

3 Results and Discussion

According to Verlee et al. [34], the packing density during the printing process is an intermediate value between bulk density and tap density. The packing density is indeed related to the flowability,

the morphology and the size of the powder. For a monosized PSD, the theoretical packing density is 64% [51], but it decreases as the powder size reduces, due to the increasing effects of interparticle friction, and electrostatic and Van der Waals forces, as the specific surface area of the particles increases [4,52–54].

The printing strategies chosen for this study resulted in an actual powder bed density of 54.23% for the 50 μm and 50.02% for the 100 μm layer thickness [55].

3.1 Debinding

During the debinding and sintering stages, the binder must be removed to avoid carbon enrichment leading to the precipitation of detrimental secondary phases that can modify the microstructure and performance of the final object.

Figure 1a shows the results of TGA carried out on a pure binder sample. It is revealed that the residual amount of binder constituents found after the TGA cycle was around 5.6% in Ar/H_2 gas mixture and 0.5% in air. From the graphs, it can be noticed that three transition stages occur during the process in air, in accordance with results published by Do et al. [32]. The first stage occurs in the 50 – 300 °C range, a second one up to about 480 °C and a third one above 570 °C. The first two stages are also found in the Ar/H_2 gas mixture with limited modifications in their temperature ranges, while the last stage is missing. It can be reasonably assumed that the third stage corresponds to the oxidation and removal of residual by-products coming from the previous degradation stages, which cannot react in the inert atmosphere. Figure 1b refers to thermogravimetric tests carried out on green samples. The results confirm the reduced efficiency of the debinding process in inert atmosphere, keeping into consideration that the binder loss in air is compensated by the weight gain induced by the oxidation, as highlighted by the change in the curve slope between 350 – 475 °C and by the subsequent weight increase.

Even though debinding was not completed using an inert atmosphere, such option was preferred for the treatment of the testing samples for two main reasons:

- oxidation of the metallic powder is prevented, thus favoring the following sintering and densification stages of the samples and even allowing the use of vacuum sintering instead of a reducing atmosphere in the following thermal cycles;
- the residual binder after Ar-debinding should be about 0.02 wt.%, given that the 94.4 wt.% of binder removed corresponds to a 0.4 wt.% loss for the green specimen, thus its effect on the microstructure could be negligible.

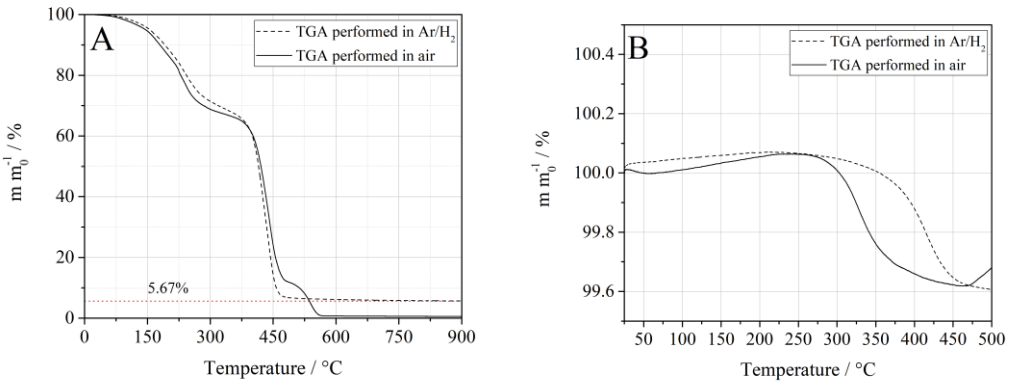

Fig. 1 Thermogravimetric curves of a) the solidified binder in inert atmosphere and air; b) green samples in inert atmosphere and air

The residual carbon analyses on samples debinded at 470 °C in the two atmospheres revealed that there is a large difference in the carbon concentration of the brown samples, namely after debinding, before sintering: 0.02 wt.% (air-debinded, which substantially corresponds to the original carbon content in the feedstock powder) and 0.13 wt.% (Ar-debinded). The complete burning of polymer is assured only for air-treated samples. In the second case, the increase in carbon is larger than expected from the results of the thermogravimetric results, which could be due to the less efficient removal of debinding by-products from green components compared to the pure binder. However, similar increases were observed also by Nandwana et al. in absence of an oxidizing atmosphere [56].

3.2 Characterization of the green samples

The green relative density values can be observed in Figure 2. By increasing the layer thickness, the relative density of the specimen decreases by ~5% due to the higher risk of macro-void formation during powder deposition and the heterogeneous binder diffusion through the structure because a larger amount of liquid is deposited on top of each layer [57,58]. Indeed, even though corresponding BS are related to the same amount of binder introduced in the specimen, capillary-induced infiltration alone does not guarantee that the binder is equally distributed within the layer in case of different LT [58]. Instead, an increase of binder saturation does not significantly affect relative density of green parts because the binder mass is minimal and its effect on the overall sample weight is negligible.

The results of the three-point bending tests on green samples are also plotted in Figure 2. It is shown that an increase in the binder content of samples leads to improved strength. This is an expected result considering that at this stage the compact strength is only provided by the polymeric binder network. Additionally, it can be noticed that there is a positive correlation between relative density and mechanical strength: the closer the particles are packed, the easier should be the formation of a continuous and thicker polymeric network connecting them [58]. Finally, it is to remark that none of the tested conditions revealed to be critical for sample handling.

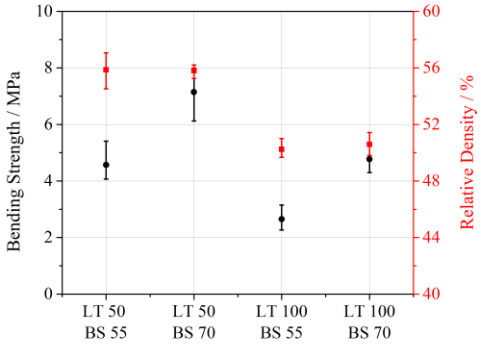

Fig. 2 Variation of bending strength and relative density of the green samples depending on the layer thickness (LT) and binder saturation (BS)

3.3 Microstructural analysis of the sintered samples

The sintering conditions were kept constant for all samples under investigation, with a holding temperature of 1360 °C (reached by a heating rate of 5 °C min^{-1}) and a soaking time of 3 h under a vacuum atmosphere at 10^{-1} mbar. As already mentioned, vacuum sintering was preferred because low amount of residual oxides are expected after the Ar debinding, and it should prevent the formation of gas-filled closed pores, that would hinder full densification.

Thermo-Calc simulations (Figure 3) was used to evaluate the effect of C due to residual binder contamination. Specifically, a comparison was drawn between the 316L steel containing the nominal amount of C of 0.03 wt.%, and a carbon-enriched steel with same chemical composition with 0.13 wt.% of C, corresponding to the results showed in section 3.1.

The increased amount of carbon has multiple effects on stability of phases. First, it lowers the liquid-formation threshold from 1400 °C to about 1360 °C, promoting the achievement of supersolidus liquid sintering. This might be an advantage since it accelerates diffusion of the alloying elements toward the solid γ and δ phases and promotes the pore-filling effect, thus enhancing densification [34,56]. The second effect of the larger C content is the stabilization of the austenite as opposed to the formation of δ-ferrite, with the latter going from about 0.7 to 0.5 molar fraction at its peak, according to thermodynamic simulation under equilibrium hypothesis (Figure 3). This might influence sintering given its dependence on self-diffusion of iron, which is faster in the BCC structure of ferrite than the more compact FCC lattice of austenite [59]. Regarding other compounds, an important advantage of the excess carbon is the reduction in the formation of the σ-phase, which is brittle and it would worsen the mechanical performance of the material. Unfortunately, as expected, the increase in carbon leads to the formation of carbides ($M_{23}C_6$), specifically with Cr. This could raise the risk of intergranular corrosion and loss of toughness when comparing properties to those of more conventional wrought 316L steels.

The thermograms obtained from DSC displayed in Figure 4 are useful to compare the behavior of the printed specimens to that predicted by Thermo-Calc simulations. On one side, the curves

obtained during heating (orange lines) confirms that early liquid formation occurs in all cases at about 1358-1359 °C. On the other hand, cooling curves (blue lines) highlight δ to γ transformation at temperatures consistent with those of standard 316L stainless steel, thus with standard carbon content. However, it should be noted that the heating ramp of the DSC reproduces accurately that of the sintering process, while the cooling rate is much lower than the actual one (-30 °C min^{-1} vs -500 °C min^{-1}), due to operational limit. This might lead to inaccuracies in the reproduction of the transformation occurring at this stage.

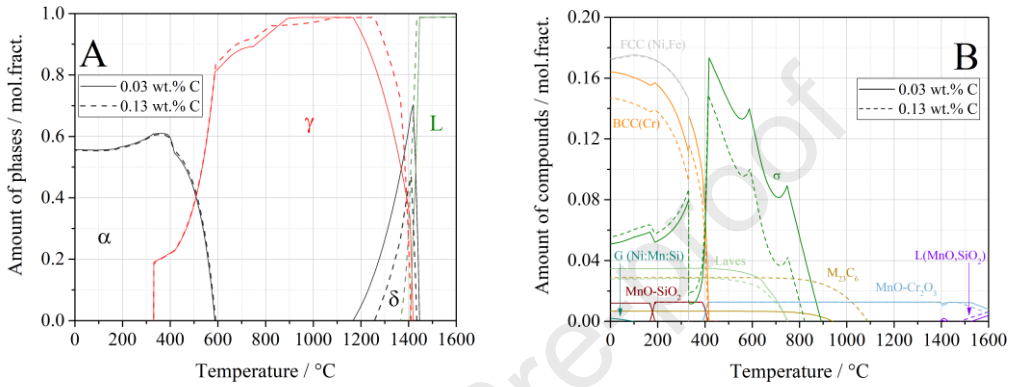

Fig. 3 Thermo-Calc equilibrium simulations of phases (a) and compounds (b) formation for the investigated steel containing 0.03 wt.% (straight line) or 0.13 wt.% (dotted line) carbon

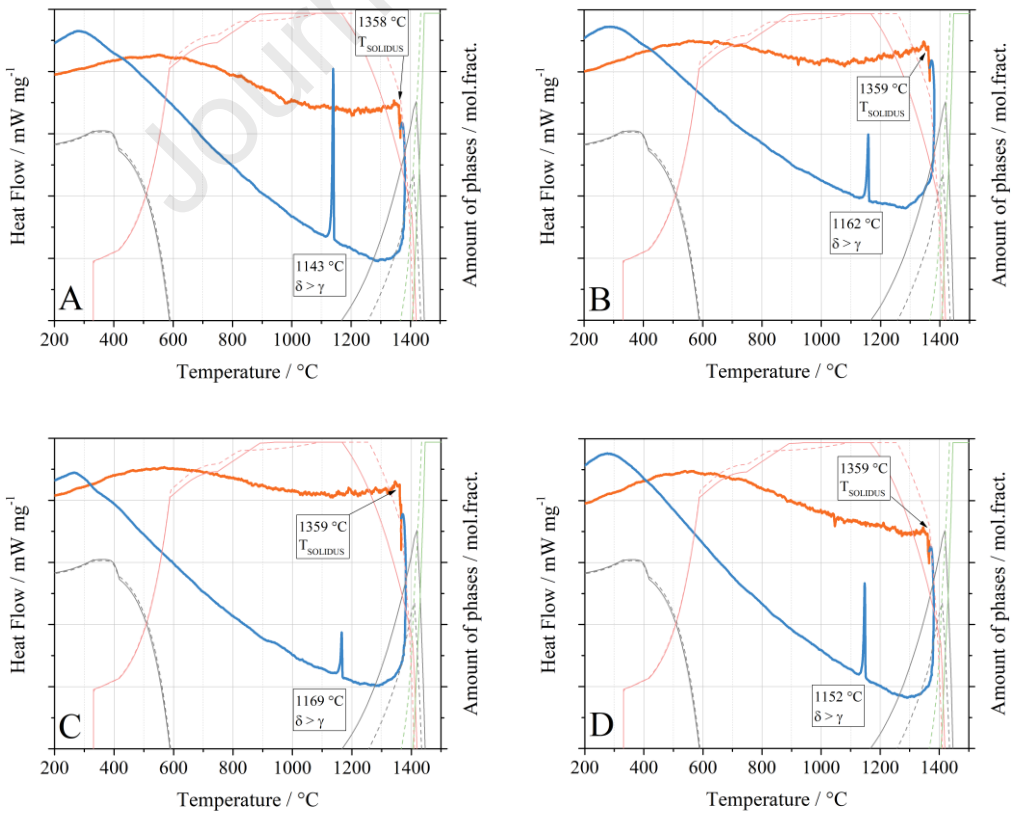

Fig. 4 Thermo-Calc equilibrium simulations of phases and DSC thermograms (bold lines) of samples (a) 55BS 50LT; (b) 70BS 50LT; (c) 55BS 100LT; (d) 70BS 100LT

Table 5 summarizes the microstructural properties after sintering of the samples obtained by the four printing conditions here investigated, while Figure 5 depicts the general features of the microstructure. From the table it can be noticed that the difference in density between samples printed with 50LT and 100LT is still present, although it is reduced with respect to the green samples. On the contrary, small density differences arise between samples with the same layer thickness but different binder saturations, in particular for the 100LT samples. This is likely due to the excess porosity in the inner region of the 70BS samples, possibly generated by the larger amount of binder that is removed during debinding. In addition, the 100LT70BS sample also displays a larger amount of unsintered particles.

As can be seen from the set of micrographs shown in Figure 5, internal porosity in all samples is extremely limited, characterized by a spherical shape, a size in the range 1-20 μm, and homogeneously distributed in the matrix, both inside grains and at grains boundaries. The small-size intragranular pores are extremely difficult to annihilate without pressure-aided sintering, thus the value of 99% relative density should be considered as a reasonable upper densification limit under these conditions [60,61]. Indeed, densities near or above 99% have been achieved only with sintering aids by Do et al. [31] and with extensive liquid sintering by Verlee et al. [34], at the cost of loss of shape accuracy. Inclusions are rare or absent. In addition, the microstructure features equiaxed austenitic grains decorated by δ-ferrite (Figure 7), as confirmed by EDX measurements reported in Table 6 and by XRD results in Figure 6, and annealing twins [62,63]. The presence of ferrite is not uncommon in this kind of stainless steel, in particular when the components are obtained by BJ [6,28]. In these cases, skeletal δ-ferrite is evident, as it can reach about 10 vol.%, and it is concentrated at the grain boundaries [28,64,65]. On the contrary, components produced by high energy additive techniques, as L-PBF, seems to feature a higher content of austenite due to the presence of ferrite of lathy and acicular shape within the austenite matrix, which can be detected only with specific inspection by EBSD or TEM [66,67]. The difference is mainly due to the solidification rates involved in the two additive techniques: BJ features a moderate cooling rate that allows diffusion of austenite-promoting elements, typically Ni and C, in the γ-matrix and ferrite-promoting elements, as Cr and Mo, at the grain borders (see Figure 8); instead, cooling rates from 10^3-10^8 °C s^{-1} are observed during L-PBF, which prevent diffusive processes to allow a redistribution of different elements within the material, thus inducing the formation of δ-phase within the austenite matrix [68–70]. Saeidi et al. observed that skeletal ferrite can form also in L-PBF samples only as result of a heat treatment above 1000 °C, thus allowing diffusion mechanisms to occur [71].

The linear shrinkage values calculated in the three directions confirm that the powder packing in the 100LT samples is lower, thus the number of voids to be filled during the sintering treatment and the

resulting shrinkage is larger. In addition, it can be noticed that the shrinkage along the building direction is higher because of improper powder packing between layers [27,48,72,73].

It can be noticed that the 50LT samples feature lower shrinkage and larger grain size. This might be explained by considering the competitive mechanisms of grain coarsening and material densification, dependent on pore size distribution. Therefore, we can identify two scenarios to explain the microstructure evolution found in the investigates samples:

1. Homogeneous distributions of small pores (50LT) due to high green packing, are easily annihilated right at the onset of the sintering, thus promoting densification and earlier grain growth.
2. Wider pore size distribution including macro-voids (100LT) experience the fast closure of the small pore fraction, but the persistent presence of the larger voids (see Figure 5d). Consequently, grain coarsening is hindered for most of the holding time and shrinkage at the end of the process can become larger, assuming macropores can eventually be annihilated.

The variation of the binder saturation seems to affect mainly the grain growth, rather than the shrinkage. It can be considered that the presence of the liquid phase (promoted by a higher carbon content) enhances the diffusion process of austenitizing elements (Ni and C above all), thus favoring grain coarsening [56,71]. However, in the present investigation, the measured grain growth was not excessive, considering that the grain size is only 3-4 times larger than the coarser powder particles (d_{90}). An additional effect that can be observed in Figure 7, is the formation of grain boundaries with rounded profile that better accommodate the liquid phase and are typical of this type of sintering mechanism [74].

The XRD spectra in Figure 6b confirm the observations made on the austenitizing effect of carbon residuals, as can be seen from the differences between samples with different BS. However, LT also seems to be effective in this regard. Most likely, the thickening of the liquid channels consequent to grain coarsening, combined to the lower carbon residuals, allows the stabilization of larger amount of ferrite within the material during the cooling stage [75].

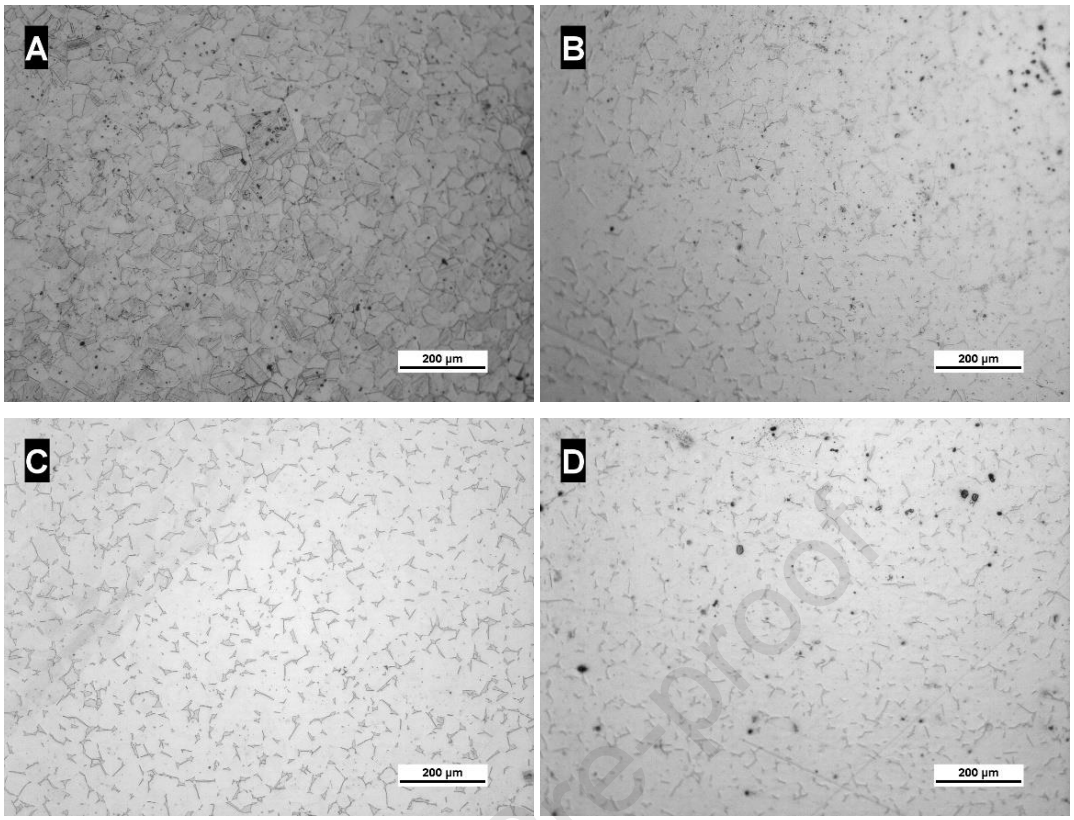

Fig. 5 Optical micrographs of samples: a) 55BS 50LT; b) 70BS 50LT; c) 55BS 100LT; d) 70BS 100LT after sintering

Table 5 Average values of relative density, shrinkage, and grain size of the sintered samples

	55BS 50LT	70BS 50LT	55BS 100LT	70BS 100LT
Density / %	98.33 ± 0.02	97.66 ± 0.02	97.54 ± 0.04	95.78 ± 0.07
Shrinkage X / %	15.07 ± 0.74	14.13 ± 0.54	16.15 ± 0.17	14.77 ± 0.35
Shrinkage Y / %	15.75 ± 0.23	14.99 ± 0.04	16.96 ± 0.44	15.25 ± 0.45
Shrinkage Z / %	17.48 ± 0.45	16.48 ± 0.20	20.05 ± 0.97	17.59 ± 0.20
Grain size / µm	34.99 ± 3.77	37.82 ± 2.91	28.95 ± 2.63	33.10 ± 3.02

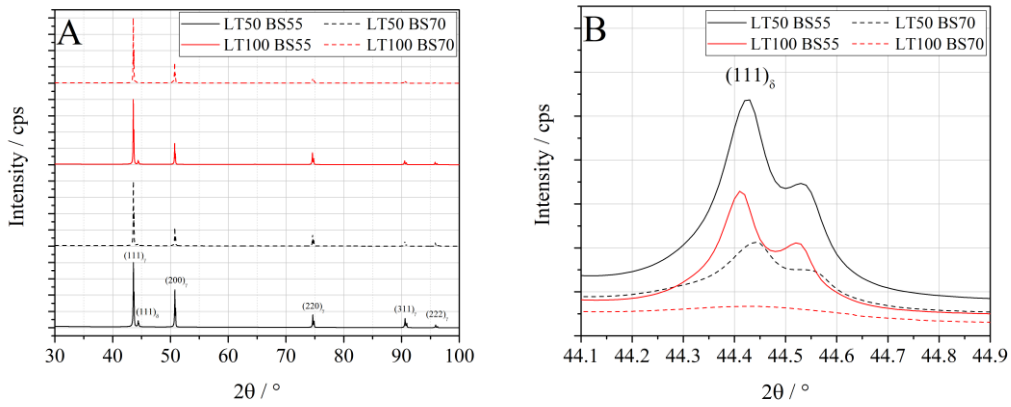

Fig. 6 XRD spectra of the sintered samples with (a) the identification of the γ and δ phase peaks and (b) the magnification of the $(111)_\delta$ peak to display the variation depending on the printing conditions

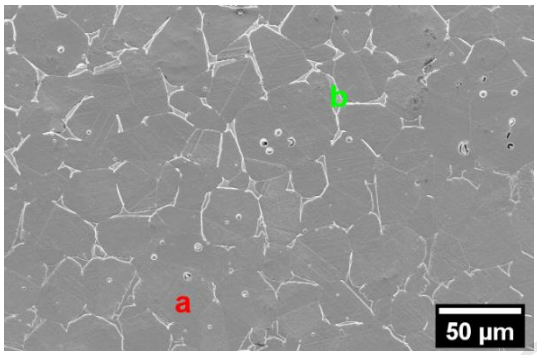

Fig. 7 SEM micrograph of a 55BS50LT sample with reference points of the EDX analysis

Table 6 Composition (wt.%) measured by EDX of the areas highlighted in Figure 6

Area	Phase	Si	Cr	Mn	Fe	Ni	Mo
a	γ	0.48	17.39	1.70	67.89	10.83	1.70
b	δ	0.53	24.01	1.56	64.61	5.33	3.83

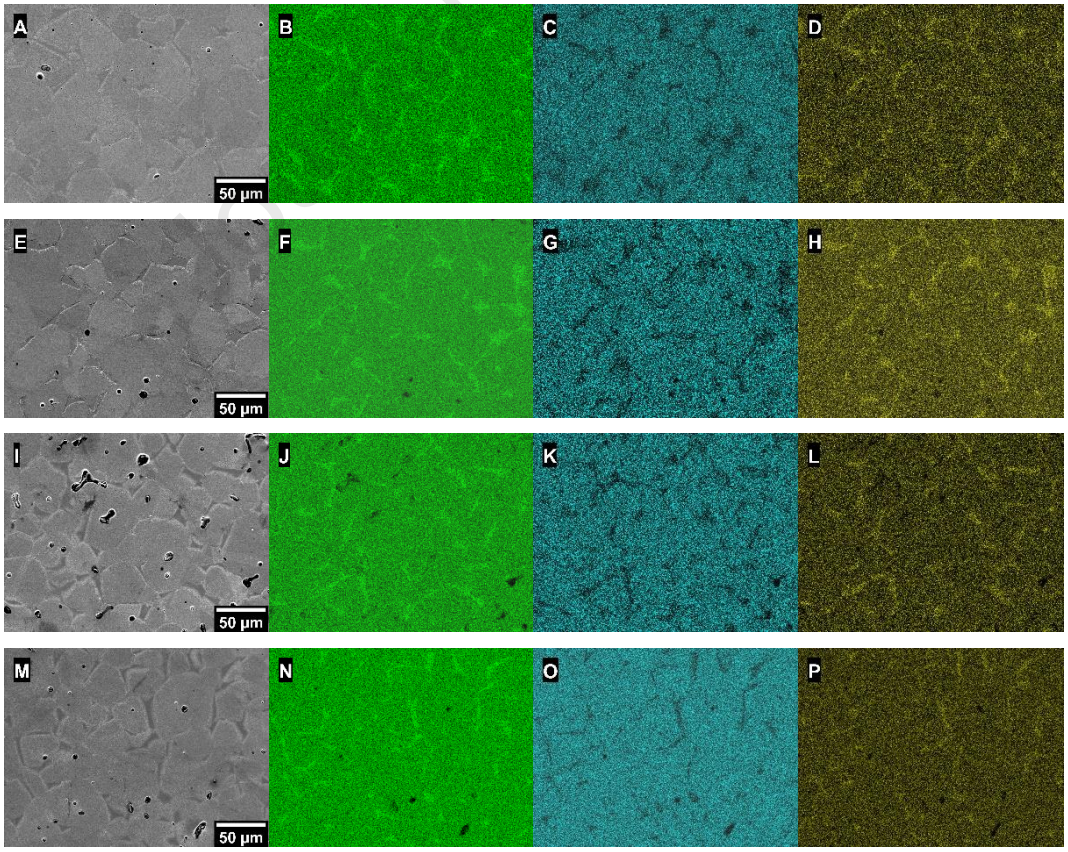

Fig. 8 EDX-SEM maps of micrographs taken from samples: (a,b,c,d) 55BS 50LT; (e,f,g,h) 70BS 50LT; (i,j,k,l) 55BS 100LT; (m,n,o,p) 70BS 100LT. Green images (b,f,g,n) displays the Cr

concentrations. Blue images (c,g,k,o) displays the Ni concentrations. Yellow images (d,h,l,p) displays the Mo concentrations.

3.4 Mechanical characterization of sintered samples

The average microhardness values and the standard deviations are summarized in Table 7. Overall, the values measured are proportional to the grain size of the corresponding printing conditions, coherently with the Hall-Petch strengthening mechanism.

These results are comparable to those published by Do et al. [31] about 316L samples produced by BJ and to cast 316L stainless steels. On the contrary it should be recalled that the same steel processed by other Laser-based Additive Manufacturing technologies (e.g. Laser-powder bed fusion), usually features much higher values due to the extremely refined microstructure, unless additional heat treatments are performed [67,71,76].

Table 7 Average values and standard deviation of Vickers hardness for the four printing conditions investigated

Sample	Vickers Hardness / HV
55BS 50LT	150 ± 9
70BS 50LT	148 ± 11
55BS 100LT	164 ± 14
70BS 100LT	150 ± 12

The results of the tensile tests are displayed in Figure 9 while the main tensile data are summarized in Table 8 and compared with properties of the 316L steel processed by other methods. A large ductility is obtained for all the BJ specimens here investigated, regardless of the printing conditions. Overall, it can be observed that the material features a similar mechanical behavior with respect to cast steel, although the yield and tensile strengths are lower. The absence of a preferred crystal orientation, of coarse pores and low inclusion content allowed to achieve fairly good combination of mechanical strength and ductility [63].

Among the four printing parameter combinations, differences are minimal. The main difference stands in the variability of fracture elongation values, and consequently of the UTS achieved, which might be due to the statistical effects of occasional pores and inclusions (see Figure 11), that could trigger the onset of the ductile fracture process in the samples. However, it can reasonably be claimed that all the investigated conditions provided a comparable behavior in the elastic and elasto-plastic regimes of the tensile curves, up to at least a strain of 40%. This is certainly an advantage at an industrial level because it demonstrates that minimal variations of the pivotal printing parameters, which may be needed to satisfy time/cost/green strength requirements for example, do not compromise the mechanical properties of the component.

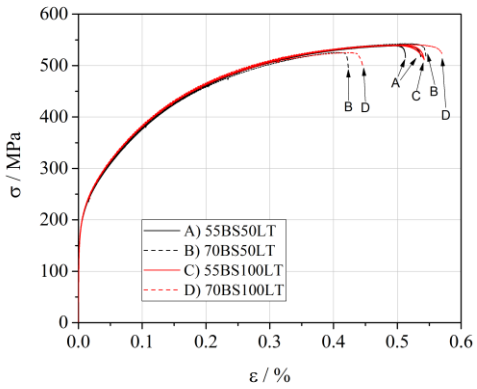

Fig. 9 Best and worst performance stress vs. strain curves obtained from the tensile tests

Table 8 Tensile properties (Yielding Strength – YS, Ultimate Tensile Strength – UTS, Maximum Elongation – ε_{max}) of specimens produced by different printing conditions, and comparison with 316L stainless steel produced by metal injection molding (MIM), Laser-powder bed fusion (L-PBF) and with standard annealed cast bar from ASTM A276/A276M - 17 standard

	YS	**UTS**	**ε_{max}**
	MPa	MPa	%
55BS 50LT	175 ± 1	540 ± 1	53 ± 1
70BS 50LT	176 ± 1	535 ± 9	49 ± 7
55BS 100LT	175 ± 3	540 ± 1	55 ± 1
70BS 100LT	174 ± 1	534 ± 8	51 ± 7
MIM [77]	~200	410 ± 18	22 ± 1
L-PBF [70]	554 ± 5	685 ± 5	36 ± 2
L-PBF [78]	423 ± 3	695 ± 3	41 ± 2
Cast 316L [79]	310	620	50

The typical features of ductile materials have been observed on the fracture surface of all the samples tested (Figure 10a). In few specific cases, microvoids may have nucleated from the rare inclusions and brittle phases that can be found in some samples, particularly those with higher binder saturation where residual oxygen and carbon after debinding was more significant, as reported in Figure 11. However, the presence of these detrimental phases is so low that effects on the overall mechanical behavior of the samples was not observed. Indeed, most of the larger voids have likely formed from pre-existing porosity, as show in Figure 10b.

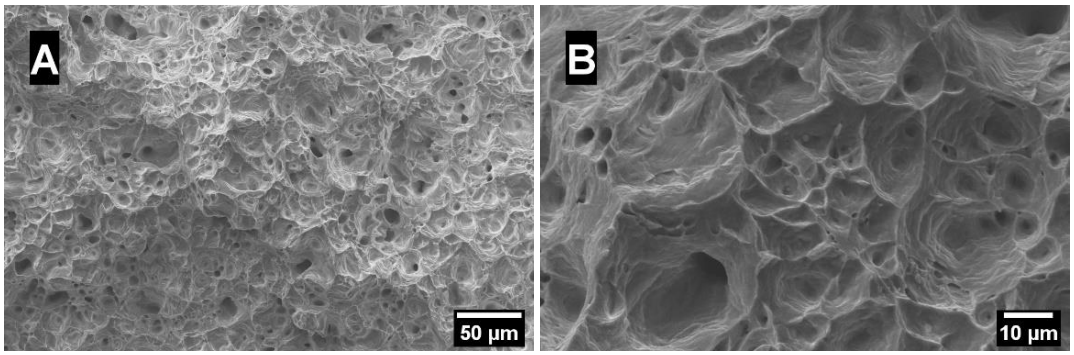

Fig. 10 SEM images of the fracture surface of the tensile specimens at different magnifications

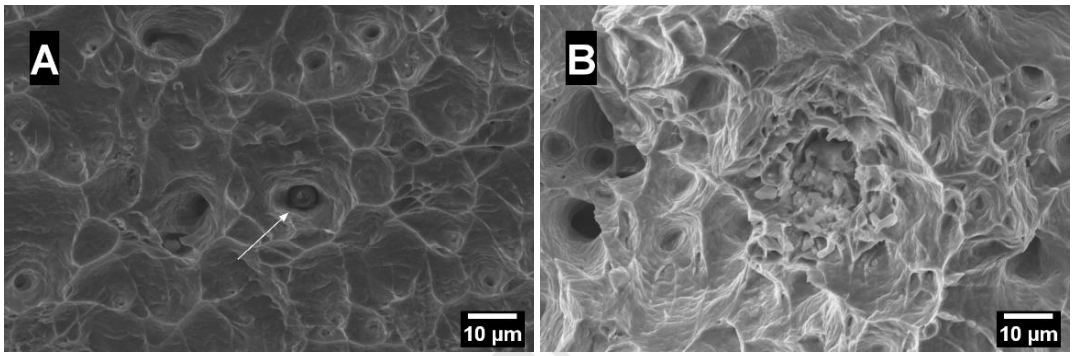

Fig. 11 SEM images of a rounded Cr-Mn-oxide inclusion (a) and an irregular micro-void likely produced by an Al-Cr-rich brittle phase (b)

4 Conclusions

In the present work, the effects of processing parameters on the microstructure and mechanical behavior of a type 316L stainless steels produced by Binder Jetting have been investigated. The influence of layer thickness and binder saturation, as well as debinding and sintering atmospheres were mainly considered. The following conclusions can be drawn.

Argon-debinding reduces the oxidation of powders and allows achieving final densities above 98% after vacuum sintering. More importantly, this avoids the need of using hydrogen or hydrogen-containing gas mixtures as sintering atmospheres, thus reducing safety and cost concerns. Vacuum sintering, in its turn, minimizes the risk of gas entrapment allowing further densification, without the need for sintering aids or longer dwelling times.

By increasing the binder saturation, inhomogeneities in both microstructure and mechanical behavior are observed, especially when high values of layer thickness are set, due to the higher presence of residual carbon resulting in the debinded samples and poor powder packing. The mechanism of binder infiltration and its effect on the sintering process should be carefully considered when planning the printing campaign, particularly in the case of complex geometries and variable thicknesses. However, it should be noted that optimal mechanical performances are obtained with different combinations of printing parameters, which gives a large degree of flexibility in the production procedure for this kind of material. For example, increasing BS might be slightly

detrimental to the final density of the specimen and generates a larger number of inclusions and pores; however, it produces comparable mechanical performances of the sintered component and more resistant green specimens, which could withstand more stressful de-powdering procedures. Such a degree of freedom is uncommon in additive manufacturing techniques and it makes binder jetting even more suitable for industrialization.

Binder Jetting is a complex technique, that can be successfully implemented only through a complete analysis of all the process and post-processing parameters, following the evolution of the microstructure for both the green and sintered samples. Their optimization is fundamental to produce reliable products showing features that cannot be obtained with other additive techniques, given the advantage of a microstructure with equiaxed grains and almost orientation-independent mechanical properties.

Acknowledgements

Authors would like to acknowledge the "Functional Sintered Materials (Funtasma)" Interdepartmental Laboratory of Politecnico di Milano, where this research activity was partially developed.

Support by the Italian Ministry for Education, University and Research through the project Department of Excellence LIS4.0 (Integrated Laboratory for Lightweight e Smart Structures) is also acknowledged.

Finally, authors would like to acknowledge the support given by Marawan Abdelwahed for the computer simulation by ThermoCalc AB Software and the evaluation of the obtained results.

Funding

This research did not receive any specific grant from funding agencies in the public, commercial, or not-for-profit sectors.

Data availability

The raw/processed data required to reproduce these findings cannot be shared at this time as the data also forms part of an ongoing study.

References

[1] E. Sachs, M. Cima, J. Cornie, Three-Dimensional Printing: Rapid Tooling and Prototypes Directly from a CAD Model, CIRP Ann. 39 (1990) 201–204. https://doi.org/10.1016/S0007-8506(07)61035-X.

[2] S.A. Uhland, R.K. Holman, M.J. Cima, E. Sachs, Y. Enokido, New Process and Materials Developments in 3-Dimensional Printing, 3DP ™, MRS Proc. 542 (1998) 153. https://doi.org/10.1557/PROC-542-153.

[3] H. Fayazfar, M. Salarian, A. Rogalsky, D. Sarker, P. Russo, V. Paserin, E. Toyserkani, A

critical review of powder-based additive manufacturing of ferrous alloys: Process parameters, microstructure and mechanical properties, Mater. Des. 144 (2018) 98–128. https://doi.org/10.1016/j.matdes.2018.02.018.

[4] M. Ziaee, N.B. Crane, Binder jetting: A review of process, materials, and methods, Addit. Manuf. 28 (2019) 781–801. https://doi.org/10.1016/j.addma.2019.05.031.

[5] T. Dahmen, C.G. Klingaa, S. Baier-Stegmaier, A. Lapina, D.B. Pedersen, J.H. Hattel, Characterization of channels made by laser powder bed fusion and binder jetting using X-ray CT and image analysis, Addit. Manuf. 36 (2020) 101445. https://doi.org/10.1016/j.addma.2020.101445.

[6] M. Nastac, R. Lucas, A. Klein, Microstructure and Mechanical Properties Comparison of 316L Parts Produced By Different Additive Manufacturing Processes, Proc. 28th Annu. Int. Solid Free. Fabr. Symp. (2017) 332–341.

[7] A. Mostafaei, A.M. Elliott, J.E. Barnes, F. Li, W. Tan, C.L. Cramer, P. Nandwana, M. Chmielus, Binder jet 3D printing—Process parameters, materials, properties, modeling, and challenges, Prog. Mater. Sci. 119 (2021) 100707. https://doi.org/10.1016/j.pmatsci.2020.100707.

[8] R.K. Mudanyi, C.L. Cramer, A.M. Elliott, K.A. Unocic, Q. Guo, D. Kumar, W-ZrC composites prepared by reactive melt infiltration of Zr2Cu alloy into binder jet 3D printed WC preforms, Int. J. Refract. Met. Hard Mater. 94 (2021) 105411. https://doi.org/10.1016/j.ijrmhm.2020.105411.

[9] T. Koyanagi, K. Terrani, S. Harrison, J. Liu, Y. Katoh, Additive manufacturing of silicon carbide for nuclear applications, J. Nucl. Mater. 543 (2021) 152577. https://doi.org/10.1016/j.jnucmat.2020.152577.

[10] S. Cao, F. Xie, X. He, C. Zhang, M. Wu, Postprocessing Study for the Controllable Structures of Ceramic Green Parts Realized by a Flexible Binder Jetting Printing (BJP) Solution, Adv. Mater. Sci. Eng. 2020 (2020) 1–17. https://doi.org/10.1155/2020/3865752.

[11] Z. Xu, Z. Zhu, P. Wang, G.K. Meenashisundaram, S.M.L. Nai, J. Wei, Fabrication of porous CoCrFeMnNi high entropy alloy using binder jetting additive manufacturing, Addit. Manuf. 35 (2020) 101441. https://doi.org/10.1016/j.addma.2020.101441.

[12] H. Miyanaji, K.M. Rahman, M. Da, C.B. Williams, Effect of fine powder particles on quality of binder jetting parts, Addit. Manuf. 36 (2020) 101587. https://doi.org/10.1016/j.addma.2020.101587.

[13] M. Mariani, R. Beltrami, P. Brusa, C. Galassi, R. Ardito, N. Lecis, 3D printing of fine alumina powders by binder jetting, J. Eur. Ceram. Soc. (2021). https://doi.org/10.1016/j.jeurceramsoc.2021.04.006.

[14] M. Mariani, I. Goncharov, D. Mariani, G. Pietro De Gaudenzi, A. Popovich, N. Lecis, M. Vedani, Mechanical and microstructural characterization of WC-Co consolidated by binder jetting additive manufacturing, Int. J. Refract. Met. Hard Mater. 100 (2021) 105639.

https://doi.org/10.1016/j.ijrmhm.2021.105639.

[15] A. Curodeau, E. Sachs, S. Caldarise, Design and fabrication of cast orthopedic implants with freeform surface textures from 3-D printed ceramic shell, J. Biomed. Mater. Res. 53 (2000) 525–535. https://doi.org/10.1002/1097-4636(200009)53:5<525::AID-JBM12>3.0.CO;2-1.

[16] F. Yang, Y. Tang, Y.F. Zhao, Manufacturability of Overhang Structures Fabricated by Binder Jetting Process, in: Vol. 2 Adv. Manuf., American Society of Mechanical Engineers, 2016. https://doi.org/10.1115/IMECE2016-65927.

[17] E.M. Wilts, T.E. Long, Sustainable additive manufacturing: predicting binder jettability of water-soluble, biodegradable and recyclable polymers, Polym. Int. 70 (2021) 958–963. https://doi.org/10.1002/pi.6108.

[18] Y. Xia, Z. Dong, X. Guo, Q. Tian, Y. Liu, Towards a circular metal additive manufacturing through recycling of materials: A mini review, J. Cent. South Univ. 27 (2020) 1134–1145. https://doi.org/10.1007/s11771-020-4354-6.

[19] N.B. Crane, Impact of part thickness and drying conditions on saturation limits in binder jet additive manufacturing, Addit. Manuf. 33 (2020) 101127. https://doi.org/10.1016/j.addma.2020.101127.

[20] R.K. Enneti, K.C. Prough, Effect of binder saturation and powder layer thickness on the green strength of the binder jet 3D printing (BJ3DP) WC-12%Co powders, Int. J. Refract. Met. Hard Mater. 84 (2019) 104991. https://doi.org/10.1016/j.ijrmhm.2019.104991.

[21] H. Chen, Y.F. Zhao, Process parameters optimization for improving surface quality and manufacturing accuracy of binder jetting additive manufacturing process, Rapid Prototyp. J. 22 (2016) 527–538. https://doi.org/10.1108/RPJ-11-2014-0149.

[22] M. Mariani, R. Beltrami, F. Meneghetti, D. Azzolini, N. Lecis, Effect of printing parameters on the mechanical strength of green body from binder jetting additive manufacturing, in: Procedia Eur. 2020 Int. Powder Met. Virtual Congr. Exhib., EPMA, 2020.

[23] R.K. Enneti, K.C. Prough, T.A. Wolfe, A. Klein, N. Studley, J.L. Trasorras, Sintering of WC-12%Co processed by binder jet 3D printing (BJ3DP) technology, Int. J. Refract. Met. Hard Mater. 71 (2018) 28–35. https://doi.org/10.1016/j.ijrmhm.2017.10.023.

[24] M. Padmakumar, Additive Manufacturing of Tungsten Carbide Hardmetal Parts by Selective Laser Melting (SLM), Selective Laser Sintering (SLS) and Binder Jet 3D Printing (BJ3DP) Techniques, Lasers Manuf. Mater. Process. 7 (2020) 338–371. https://doi.org/10.1007/s40516-020-00124-0.

[25] Y. Bai, C. Wall, H. Pham, A. Esker, C.B. Williams, Characterizing Binder–Powder Interaction in Binder Jetting Additive Manufacturing Via Sessile Drop Goniometry, J. Manuf. Sci. Eng. 141 (2019) 011005. https://doi.org/10.1115/1.4041624.

[26] H.N. Emady, D. Kayrak-Talay, W.C. Schwerin, J.D. Litster, Granule formation mechanisms and morphology from single drop impact on powder beds, Powder Technol. 212 (2011) 69–79. https://doi.org/10.1016/j.powtec.2011.04.030.

[27] M. Zago, N.F.M. Lecis, M. Vedani, I. Cristofolini, Dimensional and geometrical precision of parts produced by binder jetting process as affected by the anisotropic shrinkage on sintering, Addit. Manuf. 43 (2021) 102007. https://doi.org/10.1016/j.addma.2021.102007.

[28] P. Kumar, R. Jayaraj, J. Suryawanshi, U.R. Satwik, J. McKinnell, U. Ramamurty, Fatigue strength of additively manufactured 316L austenitic stainless steel, Acta Mater. 199 (2020) 225–239. https://doi.org/10.1016/j.actamat.2020.08.033.

[29] I.I. Cuesta, E. Martínez-Pañeda, A. Díaz, J.M. Alegre, Cold Isostatic Pressing to Improve the Mechanical Performance of Additively Manufactured Metallic Components, Materials (Basel). 12 (2019) 2495. https://doi.org/10.3390/ma12152495.

[30] H. Miyanaji, N. Momenzadeh, L. Yang, Effect of powder characteristics on parts fabricated via binder jetting process, Rapid Prototyp. J. 25 (2019) 332–342. https://doi.org/10.1108/RPJ-03-2018-0069.

[31] T. Do, T.J. Bauder, H. Suen, K. Rego, J. Yeom, P. Kwon, Additively Manufactured Full-Density Stainless Steel 316L With Binder Jet Printing, in: Vol. 1 Addit. Manuf. Bio Sustain. Manuf., American Society of Mechanical Engineers, 2018. https://doi.org/10.1115/MSEC2018-6681.

[32] T. Do, P. Kwon, C.S. Shin, Process development toward full-density stainless steel parts with binder jetting printing, Int. J. Mach. Tools Manuf. 121 (2017) 50–60. https://doi.org/10.1016/j.ijmachtools.2017.04.006.

[33] M. Ziaee, E.M. Tridas, N.B. Crane, Binder-Jet Printing of Fine Stainless Steel Powder with Varied Final Density, JOM. 69 (2017) 592–596. https://doi.org/10.1007/s11837-016-2177-6.

[34] B. Verlee, T. Dormal, J. Lecomte-Beckers, Density and porosity control of sintered 316L stainless steel parts produced by additive manufacturing, Powder Metall. 55 (2012) 260–267. https://doi.org/10.1179/0032589912Z.00000000082.

[35] J.A. Gonzalez, J. Mireles, S.W. Stafford, M.A. Perez, C.A. Terrazas, R.B. Wicker, Characterization of Inconel 625 fabricated using powder-bed-based additive manufacturing technologies, J. Mater. Process. Technol. 264 (2019) 200–210. https://doi.org/10.1016/j.jmatprotec.2018.08.031.

[36] A. Mostafaei, J. Toman, E.L. Stevens, E.T. Hughes, Y.L. Krimer, M. Chmielus, Microstructural evolution and mechanical properties of differently heat-treated binder jet printed samples from gas- and water-atomized alloy 625 powders, Acta Mater. 124 (2017) 280–289. https://doi.org/10.1016/j.actamat.2016.11.021.

[37] A. Mostafaei, E.T. Hughes, C. Hilla, E.L. Stevens, M. Chmielus, Data on the densification during sintering of binder jet printed samples made from water- and gas-atomized alloy 625 powders, Data Br. 10 (2017) 116–121. https://doi.org/10.1016/j.dib.2016.11.078.

[38] P. Nandwana, A.M. Elliott, D. Siddel, A. Merriman, W.H. Peter, S.S. Babu, Powder bed binder jet 3D printing of Inconel 718: Densification, microstructural evolution and challenges☆, Curr. Opin. Solid State Mater. Sci. 21 (2017) 207–218.

https://doi.org/10.1016/j.cossms.2016.12.002.

[39] S. Maleksaeedi, J.K. Wang, A. El-Hajje, L. Harb, V. Guneta, Z. He, F.E. Wiria, C. Choong, A.J. Ruys, Toward 3D Printed Bioactive Titanium Scaffolds with Bimodal Pore Size Distribution for Bone Ingrowth, Procedia CIRP. 5 (2013) 158–163. https://doi.org/10.1016/j.procir.2013.01.032.

[40] E. Sheydaeian, Z. Fishman, M. Vlasea, E. Toyserkani, On the effect of throughout layer thickness variation on properties of additively manufactured cellular titanium structures, Addit. Manuf. 18 (2017) 40–47. https://doi.org/10.1016/j.addma.2017.08.017.

[41] Y. Bai, G. Wagner, C.B. Williams, Effect of Particle Size Distribution on Powder Packing and Sintering in Binder Jetting Additive Manufacturing of Metals, J. Manuf. Sci. Eng. 139 (2017). https://doi.org/10.1115/1.4036640.

[42] A. Yegyan Kumar, Y. Bai, A. Eklund, C.B. Williams, The effects of Hot Isostatic Pressing on parts fabricated by binder jetting additive manufacturing, Addit. Manuf. 24 (2018) 115–124. https://doi.org/10.1016/j.addma.2018.09.021.

[43] Z.C. Cordero, D.H. Siddel, W.H. Peter, A.M. Elliott, Strengthening of ferrous binder jet 3D printed components through bronze infiltration, Addit. Manuf. 15 (2017) 87–92. https://doi.org/10.1016/j.addma.2017.03.011.

[44] A. Lores, N. Azurmendi, I. Agote, E. Zuza, A review on recent developments in binder jetting metal additive manufacturing: materials and process characteristics, Powder Metall. 62 (2019) 267–296. https://doi.org/10.1080/00325899.2019.1669299.

[45] Y. Wang, Y.F. Zhao, Investigation of Sintering Shrinkage in Binder Jetting Additive Manufacturing Process, Procedia Manuf. 10 (2017) 779–790. https://doi.org/10.1016/j.promfg.2017.07.077.

[46] H.-L. Juan, Effect of temperature ratio (Ts/Tm) and time on the sintering behavior of metallic 316L stainless steel coupons produced using jet-binder technology, (2017). http://d-scholarship.pitt.edu/id/eprint/31402 (accessed December 10, 2020).

[47] R. Frykholm, Y. Takeda, B.G. Andersson, R. Carlstrom, Solid state sintered 3-D printing component by using inkjet (binder) method, Funtai Oyobi Fummatsu Yakin/Journal Japan Soc. Powder Powder Metall. 63 (2016) 421–426. https://doi.org/10.2497/jjspm.63.421.

[48] S. Shrestha, G. Manogharan, Optimization of Binder Jetting Using Taguchi Method, JOM. 69 (2017) 491–497. https://doi.org/10.1007/s11837-016-2231-4.

[49] N. Lecis, R. Beltrami, M. Mariani, Binder jetting 3D printing of 316 stainless steel: influence of process parameters on microstructural and mechanical properties, Metall. Ital. 2 (2021) 31–41. https://www.researchgate.net/publication/352249008_Binder_jetting_3D_printing_of_316_stainless_steel_influence_of_process_parameters_on_microstructural_and_mechanical_properties.

[50] J.O. Andersson, T. Helander, L. Höglund, P. Shi, B. Sundman, Thermo-Calc & DICTRA,

computational tools for materials science, Calphad Comput. Coupling Phase Diagrams Thermochem. 26 (2002) 273–312. https://doi.org/10.1016/S0364-5916(02)00037-8.

[51] S.J. Gregorski, High green density metal parts by vibrational compaction of dry powder in three dimensional printing process, (1996). https://www.elibrary.ru/item.asp?id=5265679 (accessed January 11, 2021).

[52] S. Mirzababaei, S. Pasebani, A Review on Binder Jet Additive Manufacturing of 316L Stainless Steel, J. Manuf. Mater. Process. 3 (2019) 82. https://doi.org/10.3390/jmmp3030082.

[53] E.M. Sachs, M.J. Cima, M.A. Caradonna, J. Grau, J.G. Serdy, P.C. Saxton, S.A. Uhland, J. Moon, Jetting layers of powder and the formation of fine powder beds thereby, 2003.

[54] B.R. Utela, D. Storti, R.L. Anderson, M. Ganter, Development process for custom three-dimensional printing (3DP) material systems, J. Manuf. Sci. Eng. Trans. ASME. 132 (2010) 0110081–0110089. https://doi.org/10.1115/1.4000713.

[55] A.M. Elliott, A.M. Momen, M. Benedict, J. Kiggans, A Method for Measuring Powder Bed Density in Binder Jet Additive Manufacturing Process and the Powder Feedstock Characteristics Influencing the Powder Bed Density, in: Proc. ASME Int. Mech. Eng. Congr. Expo., 2016: pp. 1031–1037.

[56] P. Nandwana, R. Kannan, D. Siddel, Microstructure evolution during binder jet additive manufacturing of H13 tool steel, Addit. Manuf. 36 (2020) 101534. https://doi.org/10.1016/j.addma.2020.101534.

[57] A. Mostafaei, P.R. De Vecchis, K.A. Kimes, D. Elhassid, M. Chmielus, Effect of binder saturation and drying time on microstructure and resulting properties of sinter-HIP binder-jet 3D-printed WC-Co composites, Addit. Manuf. 46 (2021) 102128. https://doi.org/10.1016/j.addma.2021.102128.

[58] Y. Mao, J. Li, W. Li, D. Cai, Q. Wei, Binder jetting additive manufacturing of 316L stainless-steel green parts with high strength and low binder content: Binder preparation and process optimization, J. Mater. Process. Technol. 291 (2021) 117020. https://doi.org/10.1016/j.jmatprotec.2020.117020.

[59] F.S. Buffington, K. Hirano, M. Cohen, Self diffusion in iron, Acta Metall. 9 (1961) 434–439. https://doi.org/10.1016/0001-6160(61)90137-7.

[60] J.E. Burke, Role of Grain Boundaries in Sintering., J. Am. Ceram. Soc. 40 (1957) 80–85. https://doi.org/10.1111/j.1151-2916.1957.tb12580.x.

[61] A. Kumar, Y. Bai, A. Eklund, C.B. Williams, Effects of Hot Isostatic Pressing on Copper Parts Fabricated via Binder Jetting, 45th Sme North Am. Manuf. Res. Conf. (Namrc 45). 10 (2017) 935–944. https://doi.org/10.1016/j.promfg.2017.07.084.

[62] P. V. Muterlle, M. Perina, A. Molinari, Mechanical properties and corrosion resistance of vacuum sintered MIM 316L stainless steel containing delta ferrite, Powder Inject. Mould. Int. 4 (2010) 66–70.

[63] T. Tancogne-Dejean, C.C. Roth, D. Mohr, Rate-dependent strength and ductility of binder jetting 3D-printed stainless steel 316L: Experiments and modeling, Int. J. Mech. Sci. 207 (2021) 106647. https://doi.org/10.1016/J.IJMECSCI.2021.106647.

[64] D. Huber, L. Vogel, A. Fischer, The Effects of Sintering Temperature and Hold Time on Densification, Mechanical Properties and Microstructural Characteristics of Binder Jet 3D Printed 17-4 PH Stainless Steel, Addit. Manuf. 46 (2021) 102114. https://doi.org/10.1016/j.addma.2021.102114.

[65] A.F. Padilha, C.F. Tavares, M.A. Martorano, Delta ferrite formation in austenitic stainless steel castings, in: Mater. Sci. Forum, Trans Tech Publications Ltd, 2013: pp. 733–738. https://doi.org/10.4028/www.scientific.net/MSF.730-732.733.

[66] K. Saeidi, X. Gao, Y. Zhong, Z.J. Shen, Hardened austenite steel with columnar sub-grain structure formed by laser melting, Mater. Sci. Eng. A. 625 (2015) 221–229. https://doi.org/10.1016/j.msea.2014.12.018.

[67] Z. Sun, X. Tan, S.B. Tor, W.Y. Yeong, Selective laser melting of stainless steel 316L with low porosity and high build rates, Mater. Des. 104 (2016) 197–204. https://doi.org/10.1016/j.matdes.2016.05.035.

[68] D. Kianersi, A. Mostafaei, A.A. Amadeh, Resistance spot welding joints of AISI 316L austenitic stainless steel sheets: Phase transformations, mechanical properties and microstructure characterizations, Mater. Des. 61 (2014) 251–263. https://doi.org/10.1016/j.matdes.2014.04.075.

[69] D. Gu, Y.C. Hagedorn, W. Meiners, G. Meng, R.J.S. Batista, K. Wissenbach, R. Poprawe, Densification behavior, microstructure evolution, and wear performance of selective laser melting processed commercially pure titanium, Acta Mater. 60 (2012) 3849–3860. https://doi.org/10.1016/j.actamat.2012.04.006.

[70] R. Casati, J. Lemke, M. Vedani, Microstructure and Fracture Behavior of 316L Austenitic Stainless Steel Produced by Selective Laser Melting, J. Mater. Sci. Technol. 32 (2016) 738–744. https://doi.org/10.1016/j.jmst.2016.06.016.

[71] K. Saeidi, X. Gao, F. Lofaj, L. Kvetková, Z.J. Shen, Transformation of austenite to duplex austenite-ferrite assembly in annealed stainless steel 316L consolidated by laser melting, J. Alloys Compd. 633 (2015) 463–469. https://doi.org/10.1016/j.jallcom.2015.01.249.

[72] E. Mendoza Jimenez, D. Ding, L. Su, A.R. Joshi, A. Singh, B. Reeja-Jayan, J. Beuth, Parametric analysis to quantify process input influence on the printed densities of binder jetted alumina ceramics, Addit. Manuf. 30 (2019) 100864. https://doi.org/10.1016/j.addma.2019.100864.

[73] E. Wheat, G. Shanbhag, M. Vlasea, The Master Sinter Curve and Its Application to Binder Jetting Additive Manufacturing, J. Manuf. Sci. Eng. 142 (2020). https://doi.org/10.1115/1.4047140.

[74] R. Warren, Microstructural development during the liquid-phase sintering of two-phase

alloys, with special reference to the NbC/Co system, J. Mater. Sci. 3 (1968) 471–485. https://doi.org/10.1007/BF00549730.

[75] J. Liu, A. Lal, R.M. German, Densification and shape retention in supersolidus liquid phase sintering, Acta Mater. 47 (1999) 4615–4626. https://doi.org/10.1016/S1359-6454(99)00320-1.

[76] A. Yadollahi, N. Shamsaei, S.M. Thompson, D.W. Seely, Effects of process time interval and heat treatment on the mechanical and microstructural properties of direct laser deposited 316L stainless steel, Mater. Sci. Eng. A. 644 (2015) 171–183. https://doi.org/10.1016/j.msea.2015.07.056.

[77] M.F.F.A. Hamidi, W.S.W. Harun, N.Z. Khalil, M. Samykano, Microstructural comparison and mechanical properties of stainless steel 316L fabricated by selective laser melting and metal injection moulding processes, Int. J. Manuf. Technol. Manag. 33 (2019) 76–87. https://doi.org/10.1504/IJMTM.2019.100160.

[78] H.H. Alsalla, C. Smith, L. Hao, Effect of build orientation on the surface quality, microstructure and mechanical properties of selective laser melting 316L stainless steel, Rapid Prototyp. J. 24 (2018) 9–17. https://doi.org/10.1108/RPJ-04-2016-0068.

[79] ASTM International, A276/A276M-17 Standard Specification for Stainless Steel Bars and Shapes., ASTM Int. (2017). https://doi.org/https://doi.org/10.1520/A0276_A0276M-17.

- Residual carbon induces supersolidus-sintering at lower temperature
- Skeletal δ-ferrite forms at the grain boundaries of the γ-phase
- Final sintered density depends mostly on powder bed packing and layer thickness
- Incomplete binder removal is correlated to enhanced grain growth mechanism
- Ductile mechanical behavior and high elongation at break are achieved

Declaration of interests

☒ The authors declare that they have no known competing financial interests or personal relationships that could have appeared to influence the work reported in this paper.

☐The authors declare the following financial interests/personal relationships which may be considered as potential competing interests: